JOURNAL OF SPACECRAFT AND ROCKETS
Vol. 43, No. 1, January–February 2006

Linearized Aeroelastic Analysis for a Launch Vehicle in Transonic Flight Conditions

Francesco Capri* and Franco Mastroddi†
University of Rome "La Sapienza," 00184 Rome, Italy
and
Antonio Pizzicaroli‡
AVIO Propulsione Aerospaziale, Colleferro, 00034 Colleferro, Italy

The purpose of the present work is the development of a linearized aeroelastic modeling and analysis for a launch vehicle in the neighborhood of a transonic flight condition. A two-dimensional airfoil transonic case selected from the technical literature (specifically, a MBB-A3 supercritical airfoil in unsteady transonic regime) has been studied to validate the procedure for identifying the linearized unsteady aerodynamics. The present methodology has been successively performed for the system identification of the linearized aerodynamics of the VEGA European small launch vehicle in a transonic flow phase and in presence of an angle of attack. This has been achieved by performing several prescribed modal-transient boundary conditions on a Euler-based computational-fluid-dynamics code and postprocessing the input/output data in the frequency domain. Finally, both a standard eigenanalysis and an iterative eigenanalysis have been performed to study the aeroelastic stability on the linearized model of the launch vehicle in transonic flow. The nature of the methodology is quite general and can be applied in the neighborhood of any arbitrary parametric flight condition of a launch vehicle.

Nomenclature

$\boldsymbol{A}, \boldsymbol{A}_0, \boldsymbol{A}_1, \boldsymbol{A}_2$	=	aerodynamic reduced-order-model (ROM) matrices
$\boldsymbol{B}$	=	aerodynamic ROM matrix
$\boldsymbol{C}$	=	aerodynamic ROM matrix
C_{L_h}, C_{L_α}	=	derivative of lift coefficient with respect to plunge and pitch motions
C_{M_h}, C_{M_α}	=	derivative of moment coefficient with respect to plunge and pitch motions
C_p	=	pressure coefficient
$C_p^{(j)}$	=	pressure field caused by the motion of the jth mode
E	=	body elastic energy
$\boldsymbol{E}, E_{mn}$	=	generalized aerodynamic force matrix
$e_n(t)$	=	nth generalized (aerodynamic) forces
f_n	=	nth natural frequency, Hz
$\boldsymbol{K}, K_{mn}$	=	stiffness matrix and entries
$k = \omega l / V_\infty$	=	reduced frequency
l	=	reference aerodynamic length
$\boldsymbol{M}, M_{mn}$	=	mass matrix and entries
M_∞	=	flow Mach number at infinity
$\boldsymbol{n}$	=	unit normal vector outward the body surface
$q_m^t(t)$	=	input trial functions for the identification process
$q_n(t)$	=	Lagrangian coordinates
s	=	Laplace-domain variable
$\boldsymbol{t}$	=	body surface applied force
$\boldsymbol{u}(\xi^\alpha, t)$	=	body displacement vector field
V_∞	=	flow speed at infinity
$\boldsymbol{x}(\xi^\alpha, t)$	=	position vector field
α	=	index for material coordinates
κ	=	smoothness control coefficient
ξ^α	=	body material coordinates ($\alpha = 1, 2, 3$)
ρ	=	material mass density
ρ_∞	=	air mass density at infinity
$\boldsymbol{\Psi}^{(n)}$	=	nth modal shape function
ω	=	Fourier-domain variable
ω_n	=	nth angular natural frequency, rad/s

Received 9 October 2004; revision received 17 June 2005; accepted for publication 20 June 2005.

*Graduate Student, Department of Aerospace Engineering and Astronautics, Via Eudossiana 16.
†Associate Professor, Department of Aerospace Engineering and Astronautics, Via Eudossiana 16.
‡Aerospace Engineer, Colleferro Space Division, Corso Garibaldi, 22.

I. Introduction

THE static (divergence) and dynamic (flutter) linear aeroelastic stability for launch vehicles is a research field not as developed as that of the fixed wings that have deeply characterized the history of the aviation and have a research development of about 100 years.[1] The mature development of the aeroelastic analysis of the fixed wing is caused essentially by the capability of modeling 1) aerodynamics by means of linear unsteady flow conditions (linear potential flows[2]) and 2) structures by means of linear vibrations for structures. These model hypotheses are widely accepted and satisfied for most of the flight conditions of both civil and military aircraft. Therefore, many methods have been developed for linear aeroelastic stability and response analysis.[1,3–11] These procedures in time and frequency domains are actually available in many commercial codes.

Whenever the flow conditions and the vibratory amplitude of the structures violate these hypotheses (transonic flows, viscosity effects, stall, large deformation for structures, etc.), two procedures of solution are typically carried out:

1) The first procedure is a direct numerical simulation of the phenomenon (this concerns the field of computational aeroelasticity[3]) based, for example, on the use of a computational-fluid-dynamics (CFD) Navier–Stokes solver for the flow, on a finite element nonlinear solver for the dynamics of the structure, and on a suitable boundary-condition interface performing the fluid-structure interactions.[12,13] This approach is quite resource- and computer-time consuming and very difficult to be parametrically controlled. Furthermore, many simulations have to be performed to explore all of the parametric conditions of the aeroelastic systems that are to be studied.

2) The second procedure is a linearization of the flow-structure behavior around the reference condition. This linearization can be

performed in two different ways: a) by means of a linearization of the original partial-differential-equation (PDE) mathematical model (e.g., a transonic small disturbance model for the aerodynamics) and then performing a space-time discretization; or b) by means of a direct linearization of the aerodynamic numerical model by using CFD codes to produce the data necessary to perform such a linearization.[4]

The lack of validated commercial codes and experimental tests on full-scaled or scaled model[14–21] is a motivation for addressing this kind of analysis toward direct use of a numerical simulation. This is typically very expensive from a computational point of view and practically not useful in a launch vehicle (LV) design phase. Thus, in the present paper the second approach, which uses a linearized aeroelastic analysis of a LV, has been performed. Specifically, following the numerical linearization approach denoted as b, the aeroelastic analysis of a three-dimensional axial-symmetric geometry of a LV in the neighborhood of transonic flight condition with prescribed angle of attack has been performed. The aerodynamic model considered for this linearization in the neighborhood of a transonic solution can take into account possible aerodynamic instabilities such as transonic buffet. However, other typical instabilities occurring in launcher aerodynamics due, for example, to flow separation (e.g., the stall buffet) will not be considered in this study.

The transonic flight conditions examined here are considered to be a worst case from an aeroelastic point of view. Indeed, during this flight phase, the aerodynamic pressure distribution around the body can change rapidly as function of angle of attack and Mach number because of the sonic region displacement along the body profile. This allows one to retain an inviscid aerodynamic solution in order to predict the global aerodynamic loads.

The structural dynamic model has been developed using a linear modal representation for the LV structure in terms of the lowest natural frequencies and natural mode shapes of vibrations. The linearized unsteady aerodynamic model has been obtained using the CFD data given by an Euler-based code and then postprocessed to obtain a global generalized representation for the aerodynamic unsteady loads depending on the actual deformation state of the LV. More specifically, the linearized aerodynamic operator has been identified through a time-/frequency-domain analysis on the base of trial unsteady-boundary-condition input performed with shape given by the modal analysis of the LV structure. Both the structural and aerodynamic models have been finally employed in the aeroelastic coupled model given by the generalized Lagrange equations of motion. These linearized equations [time-dependent ordinary differential equations (ODE)], describing the aeroelastic behavior of the launcher, have, as unique unknowns of the problem, the modal coordinates chosen to describe the linearized motion.Finally, to check the local stability of the Vega LV an eigenanalysis (in terms of aeroelastic system poles or eigenvalues), on the linear ODE model recast in a first-order form, has been performed.

II. Theoretical Model for Linearized Aeroelasticity

The deformable body, with respect to an equilibrium position, is described by the displacement field $\boldsymbol{u}(\xi^\alpha, t)$, where $\xi^\alpha (\alpha = 1, 2, 3)$ are the material coordinates of the solid and t is time. This vector field can be decomposed in a spectral way as

$$\boldsymbol{u}(\xi^\alpha, t) = \sum_{n=1}^{\infty} \boldsymbol{\Psi}^{(n)}(\xi^\alpha) q_n(t) \tag{1}$$

where $\boldsymbol{\Psi}^{(n)}(\xi^\alpha)$ are prescribed vector fields satisfying the homogeneous boundary conditions of the body and $q_n(t)$ are the associated generalized coordinates describing the solid motion. Note that this motion description is exact if all of the theoretically infinite contributions in the summation are considered and the assumed vector-field functions $\boldsymbol{\Psi}^{(n)}(\xi^\alpha)$ have satisfied adequate properties of independence and closure in the relative function space. However, if the summation is truncated to a finite number of terms equal to M, the body system will be referred as space discretized. This hypothesis will be assumed in the present model.

Assuming the preceding position for the description of the displacement fields of the body and considering the first principles of conservation for mass, momentum, and angular momentum together with the constitutive assumption of elastic body (which is related with the energy conservation principle), the following Lagrange equations of motion around the equilibrium position can be obtained:

$$\sum_{m}^{M} M_{nm}\ddot{q}_m + \frac{\partial E}{\partial q_n} = e_n(q_n), \qquad n = 1, 2, \ldots, M \tag{2}$$

where M is the finite number of Lagrangian equations and generalized coordinates included in the analysis and

$$M_{nm} := \iiint_V \rho(\xi^\alpha)\boldsymbol{\Psi}^{(n)}(\xi^\alpha) \cdot \boldsymbol{\Psi}^{(m)}(\xi^\alpha)\, \mathrm{d}V$$

are the coefficients of the mass matrix, ρ is the solid mass density, E is the solid elastic energy, and

$$e_n = \oint_S \boldsymbol{t} \cdot \boldsymbol{\Psi}^{(n)}(\xi^\alpha)\, \mathrm{d}S \tag{3}$$

are the generalized forces obtained by projecting the body surface force field $\boldsymbol{t}$ (exerting by the flow on the body) on the function $\boldsymbol{\Psi}^{(n)}(\xi^\alpha)$. If the flow on the body surface is not viscous, then the aerodynamic surface force field is given by $\boldsymbol{t} = -\frac{1}{2}\rho_\infty V_\infty^2 C_p \boldsymbol{n}$, where ρ_∞ and V_∞ are the flow density and velocity at infinity, C_p the aerodynamic pressure on the body surface, and $\boldsymbol{n}$ the outward normal on the body surface. In this case Eq. (3) becomes

$$e_n = -\frac{1}{2}\rho_\infty V_\infty^2 \oint_S C_p(\xi^\alpha)\boldsymbol{n} \cdot \boldsymbol{\Psi}^{(n)}(\xi^\alpha)\, \mathrm{d}S \tag{4}$$

Note that these forces in the aeroelastic application typically depend on the motion, that is, on the Lagrange variables $q_n(t)$.

In the case of interest of linearized motion (e.g., this is the case of absence geometric nonlinearities for the structure and linearized potential flow for aerodynamics) around the equilibrium position, then Eq. (2) can be recast in the Laplace domain as

$$\sum_{m}^{M} s^2 M_{nm}\tilde{q}_m + \sum_{m}^{M} K_{nm}\tilde{q}_m = \frac{1}{2}\rho_\infty V_\infty^2 \sum_{m}^{M} E_{nm}(s; M_\infty, V_\infty)\tilde{q}_m \tag{5}$$

with $n = 1, 2, \ldots, M$ and where the Laplace transform functions have been indicated with the superscript symbol $\tilde{}$. K_{nm} is the stiffness matrix that models the linear portion of the structure elastic forces, M_∞ is the Mach number, and E_{nm} is the linearized unsteady aerodynamic operator [generalized aerodynamic force matrix (GAF)] typically dependent on the flow conditions (M_∞, V_∞).

If the shape functions $\boldsymbol{\Psi}^{(n)}(\xi^\alpha)$ are the standard shape functions used in the finite element (FE) method for structures, then the generalized coordinates will represent the physical degrees of freedom associated to the local FE grid nodes and K_{nm}, M_{nm} the corresponding elements of stiffness and mass matrices. Moreover, in this case the GAF matrix will linearly relate the unsteady displacements on the body surface with the consequent aerodynamic forces applied on the body surface. The magnitude of the number of such degrees of freedom can be typically of the order of thousands.

Nevertheless, assuming as a shape function $\boldsymbol{\Psi}^{(n)}(\xi^\alpha)$, the natural modes of vibrations of the structures, the generalized coordinates represent the modal coordinates and K_{nm}, M_{nm} the corresponding diagonal stiffness and mass modal matrices. Moreover, the GAF matrix in this case relates assumed mth modal motion on the body surface with the consequent projection of the aerodynamic pressure distribution on the nth shape function. Again, the magnitude of the number of such degrees of freedom is typically of the order of 10, fixing the accuracy as the same reached by the corresponding FE discretization. For this reason, in the aeroelastic application the modal

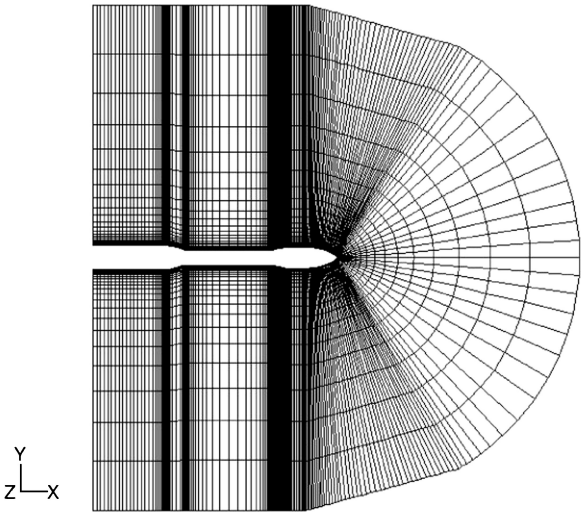

Fig. 1 Two-dimensional vision of geometry and aerodynamic structured mesh for VEGA LV.

description is widely employed when global phenomena (like stability) are the main objective of the analysis, and the computational economy for the evaluation of the GAF matrix represents a relevant issue.

The procedure to identify the linearized unsteady aerodynamic model (GAF matrix) on the basis of the CFD data and the representation of the aeroelastic system in the state-space form is presented in Secs. II.A and II.B, respectively.

A. Linearized Unsteady Aerodynamic Model (GAF Matrix)

In this subsection, the numerical procedure employed to identify the linearized unsteady aerodynamic operator in the neighborhood of a critical transonic flow condition will be shown. Figure 1 gives an idea of the VEGA LV geometry used in the following aerodynamic simulation (the launcher has a medium diameter of 3 m and a length of about 30 m) together with the aerodynamic mesh employed in the calculations. (More detailed issues on LV geometry and mesh will be given in Sec. II.B.)

In Sec. II.A.1 some issues concerning the use of modal unsteady boundary condition as input for the CFD by mean of the use of a moving mesh procedure will be presented. Next, in Sec. II.A.2, the procedure used to obtain the generalized modal forces [Eq. (4)] has been illustrated. Finally, in Sec. II.A.3 the GAF matrix has been built up.

1. Unsteady CFD Model and Moving Mesh Procedure for the Boundary Conditions

The CFD simulation has been performed with the commercial code FLUENT ver. 6.1.18 (Ref. 22). The dynamic mesh module can upgrade the nodes position of mesh during motion with three methods: 1) spring-based smoothing, 2) dynamic layering , and 3) local remeshing. In the current approach, the spring-based smoothing method has been used.

When the motion of the body surface is assigned, it can be represented in modal coordinates using Eq. (1), and the consequent impermeability condition is applied to the fluid boundary. If a surface motion is assigned with a space dependency given,for example, by the generic mth mode (see also Sec. II.A.3), the corresponding displacement field is given by

$$\boldsymbol{u}_t(\xi^\alpha, t) = \boldsymbol{\Psi}^{(m)}(\xi^\alpha) q_m^t(t) \tag{6}$$

with $q_m^t(t)$ arbitrary function defining the boundary-condition time dependency, whereas the mth modal shape defines the boundary condition in the space domain. This is equivalent to assign the boundary conditions in terms of the following set of modal coordinates:

$$\begin{bmatrix} 0 & 0 & \cdots & q_m^t(t) & 0 & \cdots & 0 \end{bmatrix}$$

where only the mth component is not zero. In this case, differentiating Eq. (6), we have

$$\mathrm{d}\boldsymbol{u}_t(\xi^\alpha, t) = \dot{q}_m(t) \boldsymbol{\Psi}^{(m)}(\xi^\alpha)\, \mathrm{d}t \tag{7}$$

Therefore, the updated position of the grid node, with material coordinate ξ^α after the time $\mathrm{d}t$, is given by

$$\boldsymbol{x}(\xi^\alpha, t + \mathrm{d}t) = \boldsymbol{x}(\xi^\alpha, t) + \dot{q}_m^t(t) \boldsymbol{\Psi}^{(m)}(\xi^\alpha)\, \mathrm{d}t \tag{8}$$

This algorithm has been implemented through a user-defined function (UDF) within the FLUENT code. At each time step the FLUENT solver calls the routine, reads and computes the displacement fields for all moving nodes, and upgrades the mesh. More issues concerning the time-step definition will be discussed in Sec. II.C.

2. Generalized Forces Obtained by Modal Projection

The pressure-coefficient field due to the unsteady boundary condition defined in space by the generic jth mode is indicated with $C_p^{(j)}(\xi^\alpha, t)$. However, this field includes a steady-state component given by the developed flow at the prescribed aerodynamic external condition. This contribution has been filtered out by subtracting it from the global pressure field because the linearized description given by the Eq. (5) includes perturbed quantities only.

Thus, the corresponding generalized aerodynamic forces can be evaluated using Eq. (4), or

$$e_n^{(j)}(t) = -\frac{1}{2}\rho_\infty V_\infty^2 \oint_S C_p^{(j)}(\xi^\alpha, t) \boldsymbol{n}(\xi^\alpha) \cdot \boldsymbol{\Psi}^{(n)}(\xi^\alpha)\, \mathrm{d}S \tag{9}$$

where $C_p^{(j)}(\xi^\alpha, t)$ here is only the evaluated unsteady perturbed part of the pressure field due to the motion associated to the jth mode shape.

The surface integral performed on the surface S in Eq. (9) of the body has been numerically performed using a zeroth-order formula considering constant every quantity in any aerodynamic panel composing the surface mesh and equal to the value at the centroid of the panel itself, that is,

$$e_n^{(j)}(t) \cong -\frac{1}{2}\rho_\infty V_\infty^2 \sum_k^{N_c} C_p^{(j)}\left(\xi_k^\alpha, t\right) \boldsymbol{n}\left(\xi_k^\alpha\right) \cdot \boldsymbol{\Psi}^{(n)}\left(\xi_k^\alpha\right) A_k \tag{10}$$

where the subscript k represents quantities evaluated at the generic kth panel centroid and A_k is the surface area of the same panel.

3. Input/Output Identification of the GAF Matrix

As stated in Eqs. (2) and (5), the linearized unsteady aerodynamic operator in the Laplace domain transforming the modal coordinates $\tilde{q}_m$ into the generalized forces $\tilde{e}_n$ is described as

$$\tilde{e}_n = \frac{1}{2}\rho_\infty V_\infty^2 \sum_m^M E_{nm}(s; M_\infty, V_\infty) \tilde{q}_m \tag{11}$$

Thus, the simplest identification procedure for the GAF matrix operator E_{nm} is knowledge based on a given output $\tilde{e}_n$ because of a prescribed input $\tilde{q}_m$. Specifically, once a suitable input trial function $\tilde{q}_m^t$ is given for the mth mode (see Sec. II.A.1, keeping all of the others equal to zero) the corresponding displacement field on the body is given by Eq. (6). Therefore, assuming this motion for the aerodynamic mesh, the corresponding pressure coefficient field is evaluated by the CFD code and, consequently, the nth generalized aerodynamic force computed by Eq. (10). After transforming this force in the Laplace domain, the GAF matrix can be identified by

$$E_{nm}(s) = \tilde{e}_n^m \Big/ \tilde{q}_m^t \tfrac{1}{2}\rho_\infty V_\infty^2 \tag{12}$$

The choice of the trial input function $\tilde{q}_m^t$ is an important issue concerning both time/frequency crossing issues and CFD time/space discretization. Indeed, this function has to satisfy the compromise to be "notch" enough in time (consequently, enough wide in frequency domain) to excite all of the modes included in the aeroelastic analysis. At the same time, it cannot have a frequency band too large

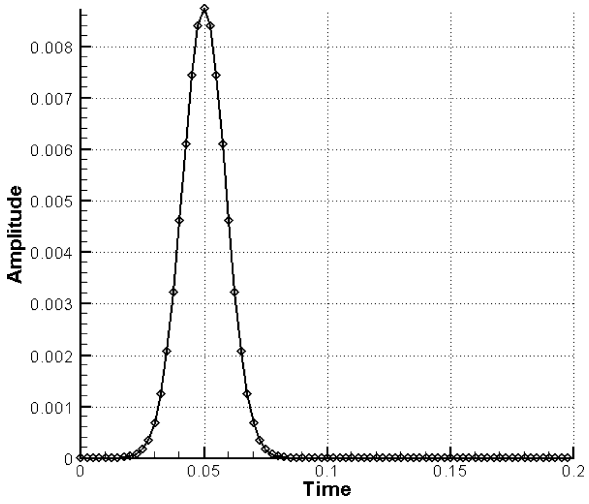

Fig. 2 Trial test function of time used for aerodynamic identification process.

to avoid inducing numerical instability and lack of accuracy for the applied CFD solver. For this purpose, the function

$$q^t(t) = C\,\exp\{-[(t - T/2)/\kappa T]^2\} \tag{13}$$

is used, where C is the notch function amplitude, T is the time window width, and κ (with $0 < \kappa < 1$) is a coefficient controlling the smoothness of the function at the boundary of its domain. Indeed, the advantage given by this function consists of the smoothness of such a function $q^t(t)$ at $t = 0$, which implies that it is here practically zero with its derivatives up to the second order. This is a relevant issue because the modal unsteady boundary conditions are given in terms of velocity of the mesh points, and therefore the smoothness of such a function is recommended.

The function parameters are determined to have a correct (in term of space-aliasing problem) unsteady flow description up to a reduced frequency (Strouhal number) of $k = 0.6$, and, finally to have an amplitude A large enough to perturb the unsteady flow but not so large to induce numerical instability or nonlinear phenomena. (Indeed, a linearization of flow condition is the objective of this work.) This function is depicted in Fig. 2. The period of time T_{app} when the function is applied is related with the frequency band to be excited: specifically, as the interested frequency band is up to around 15 Hz, it is considered $T_{\text{app}} = 0.1$s.

Finally, note that only Fourier transforms (not Laplace transforms) of signals with arbitrary shapes can be numerically performed. Therefore, substituting the Laplace transforms with the Fourier transform in Eq. (12), a frequency-response-function (FRF) GAF matrix instead of a transfer-function (TF) matrix is obtained. The FRF is obtained by the TF when the Laplace variable domain is restricted to the imaginary axis of the complex plane. This issue is relevant when related to study the stability of the aeroelastic system given by Eq. (5) as emphasized in Sec. II.B.

B. Reduced-Order Model for Linearized Aeroelasticity

Following the procedure illustrated in Sec. II.A, a linearized unsteady aerodynamic operator (GAF matrix) can be identified in the frequency domain, that is, for $s = j\omega$. Nevertheless, considering Eq. (5), the stability analysis should be performed by solving the following eigenproblem for the eigenvalues s_n and the eigenvector $\boldsymbol{u}$:

$$\left[s^2\boldsymbol{M} + \boldsymbol{K} - \tfrac{1}{2}\rho_\infty V_\infty^2 \boldsymbol{E}(s; M_\infty, V_\infty)\right]\boldsymbol{u} = 0 \tag{14}$$

where the GAF matrix should be known in all of the complex planes (any values of s). Once the eigenvalues s_n and the eigenvectors $\boldsymbol{u}^{(n)}$ are determined, the free time response of the aeroelastic system is then given by

$$\boldsymbol{q}(t) = \sum_n^M c_n \boldsymbol{u}^{(n)} e^{s_n t} + \text{complex conjugate terms} \tag{15}$$

where it is apparent (as in any standard linear analysis) that the nature of the eigenvalues s_n influences the system stability. However, the functional dependency of the operator $\boldsymbol{E}$ on the variable s is the relevant and characteristic issue of the aeroelastic problem. Indeed, this dependency is typically not of polynomial type, that is, the aerodynamic operator is not purely of differential type in time (e.g., for the linear potential aerodynamic of the fixed wing this is of transcendental type,[11]). Nevertheless, the GAF matrix $\boldsymbol{E}$ is only numerically known [see Eq. (12)] and only in the Fourier domain of $\omega = Im(s)$. Therefore, two possibilities are available for solving the nonstandard eigenproblem given by Eq. (14):

1) Use an iterative procedure to capture the eigenvalues assuming an analytic extension for the GAF matrix $\boldsymbol{E}$ from the imaginary axis on all of the complex planes.[1,11] The eigenvectors can be then evaluated by the corresponding homogeneous problem.

2) Assume an analytical structure for the GAF matrix $\boldsymbol{E}$ and then determine it in a least-square sense minimizing the error of this evaluation with respect to the GAF data known in the Fourier domain by the CFD analysis.

The first methodology is the most common approach employed in the fixed-wing aeroelastic stability analysis, and a lot of iterative eigenmethods are implemented in commercial codes (e.g., k method, p–k method, g method).[1,3,11] The second procedure has the advantage of transforming the nonstandard eigenproblem into a standard one and, as byproduct, describing the linearized aeroelastic system in a pure linear system of linear time ODE. This means that the problem is reduced in a state-space representation. This kind of methodology is referred in the aeroelastic literature as reduction of the system in a reduced-order model (ROM). Both approaches have been used in the present activity for the aeroelastic analysis.

The analytic structure of the matrix polynomial approximation used here for the fitting of the frequency-domain data for the GAF matrix is (see Refs. 8, 9, and 11 for details)

$$\boldsymbol{E}(\omega) = -(\omega^2 l^2/V^2)\boldsymbol{A}_2 + j(\omega l/V)\boldsymbol{A}_1 + \boldsymbol{A}_0 + \boldsymbol{C}[j(\omega l/V)I - \boldsymbol{A}]^{-1}\boldsymbol{B} \tag{16}$$

where the explicit dependency on the dimensionless Strouhal number $k := \omega l/V$ has been introduced because of the analogy with the theory of the unsteady linear aerodynamic of the wings. Note that $\boldsymbol{A}_2, \boldsymbol{A}_1$, and $\boldsymbol{A}_0$ are $M \times M$ square matrices, whereas $\boldsymbol{B}, \boldsymbol{A}$, and $\boldsymbol{C}$ are $N_p \times M$, $N_p \times N_p$, and $M \times N_p$ typically rectangular matrices respectively with N_p representing the assumed number of poles of the aerodynamic operator.[11] Minimizing the error between the approximating structure and the aerodynamic data of the $\boldsymbol{E}$ matrix in the frequency domain as described in Sec. II.A, the constant matrix $\boldsymbol{A}_2$, $\boldsymbol{A}_1$, $\boldsymbol{A}_0$, $\boldsymbol{B}$, $\boldsymbol{A}$, and $\boldsymbol{C}$ can be numerically identified in a least-square sense (taking special care for the evaluation of $\boldsymbol{A}$ whose eigenvalues have to be stable to ensure that the aerodynamic operator $\boldsymbol{E}$ be self-stable).

Once these matrices are built up, Eq. (16) can be analytically extended from the Fourier to the Laplace domain (i.e., $j\omega$ is substituted by s), and therefore Eq. (5) gives

$$\left(s^2\boldsymbol{M}_C + s\boldsymbol{D}_C + \boldsymbol{K}_C\right)\tilde{\boldsymbol{q}} - C\tilde{\boldsymbol{r}} = 0$$

$$s\tilde{\boldsymbol{r}} = (V/l)\boldsymbol{A}\boldsymbol{r} + (V/l)\boldsymbol{B}\tilde{\boldsymbol{q}} \tag{17}$$

with $M_C := M - \frac{1}{2}\rho_\infty l^2 A_2$, $K_C := K - \frac{1}{2}\rho_\infty V_\infty^2 A_0$, and $D_C := -\frac{1}{2}\rho_\infty V_\infty A_1$. Finally, coming back to the time domain and introducing the state-space vector $\boldsymbol{x} = \{q^T | \dot{q}^T | r^T\}^T$, the first-order linear ODE representation of the aeroelastic system can be obtained:

$$\dot{x} = \begin{bmatrix} 0 & I & 0 \\ -\boldsymbol{M}_C^{-1}\boldsymbol{K}_C & -\boldsymbol{M}_C^{-1}\boldsymbol{D}_C & q_D\boldsymbol{M}_C^{-1}\boldsymbol{C} \\ (V_\infty/l)\boldsymbol{B} & 0 & (V_\infty/l)\boldsymbol{A} \end{bmatrix} x \tag{18}$$

where $q_D := \frac{1}{2}\rho_\infty V_\infty^2$ is the dynamic pressure. Once the system is described in this form, the stability analysis is trivially reduced to a standard eigenanalysis completely based on the sign check of the real part of the eigenvalues of the final matrix in square brackets in

Eq. (18). Therefore, the iterative procedure introduced at the beginning of this section has been used to validate the results obtained by the standard eigenanalysis.

III. Validation of GAF-Matrix Identification Process

The selected test case to validate the transonic aerodynamic identification procedure is the standard AGARD supercritical MBB-A3 airfoil.[23] The linearized unsteady transonic analysis for this airfoil has been performed in Ref. 24. The aerodynamic solver employed in this reference is XTRAN2L developed at NASA Langley Research Center. It is a finite difference aerodynamic code based on a two-dimensional small-perturbation transonic unsteady potential flow model. Although the physical model in Ref. 24 is more approximate than that used in the simulations presented here, we have considered these unsteady-transonic results because they are available in the same frequency-domain form we consider in our analysis and relate directly to generalized forces.

Two different geometrical meshes have been considered in this validation study: an unstructured mesh and a structured one. Even if structured meshes typically ensure more accurate results, the moving-mesh algorithm is, on the other hand, typically more robust for the unstructured mesh. The considered airfoil geometry has been taken from AGARD standard Ref. 23, where the airfoil boundary line is given for a finite number of points. Thus, a data-point interpolation has been performed using the graphic preprocessor in GAMBIT code,[25] which is based on the NURBS algorithm. The geometry of the unstructured mesh is a standard C-type, whereas that of the structured one is a parabolic C-type.

An implicit solver for the PDE scheme has been chosen in FLUENT code not only to make the numerical convergence faster, but also because the explicit scheme for the unsteady simulation exhibited an apparent numerical instability. This issue has not been investigated in this work. The reference configuration of the undisturbed flow considered in the simulation[24] is $M_\infty = 0.79$, $\alpha = -0.5$ deg, $p_\infty = 55{,}506$ Pa, and $T_\infty = 256.98$ K. We performed a convergence analysis both for a structured and an unstructured mesh. A convergence study on the steady C_p distribution on the reference steady condition just considered has been carried out. The convergence analysis included 1) a coarse mesh with 50×40 elements in flowwise direction and orthogonal direction respectively, 2) a medium mesh with 70×60 elements, and 3) a fine mesh with 100×80 elements. From this analysis, we estimated a satisfactory performance of the mesh for the aerodynamic loads calculation from medium to fine resolution. Thus, we used the refined mesh for all steady and unsteady calculations. The steady pressure field obtained with structured mesh is represented in Fig. 3. Figure 4 shows a comparison between the predicted steady pressure coefficients on the airfoil surface (structured-mesh and unstructured-mesh cases) and those given in Ref. 24. As in Ref. 24, two rigid motions have been considered as reference shape functions for structural model (pitch and plunge motions). The pitch rotation has been performed in FLUENT code imposing the same rotation angle in any grid node through a so-called UDF. The time refresh of the grid mesh is performed by an updating spring-smoothing based method. The time test trial function is a Gaussian type (see Sec. II.A.3).

Taking the (discrete) Fourier transforms of the obtained time response and dividing these transforms by the Fourier transformed input (see Sec. II.A.3), the components of the GAF matrix can be obtained and compared with those shown in Ref. 24. Note that for a pitching-plunging airfoil, these components coincide with the aerodynamic derivatives C_{L_h}, C_{L_α}, C_{M_h}, and C_{M_α}, which gives the dynamic contribution given to lift or moment coefficients by unsteady plunge or pitch motions, respectively (specifically, e.g., the unsteady lift coefficient in frequency domain will be given by $\tilde{C}_L = C_{L_h}\tilde{h} + C_{L_\alpha}\tilde{\alpha}$). Figures 5 and 6 show the obtained results as real and imaginary parts of the aerodynamic coefficients C_{L_α} and C_{M_α} as function of the reduced frequency. The procedure for the plunge mode is the same of that used for pitch except that a larger input amplitude for the unstructured mesh can be used because the mesh can be more easily deformed. The results are in general

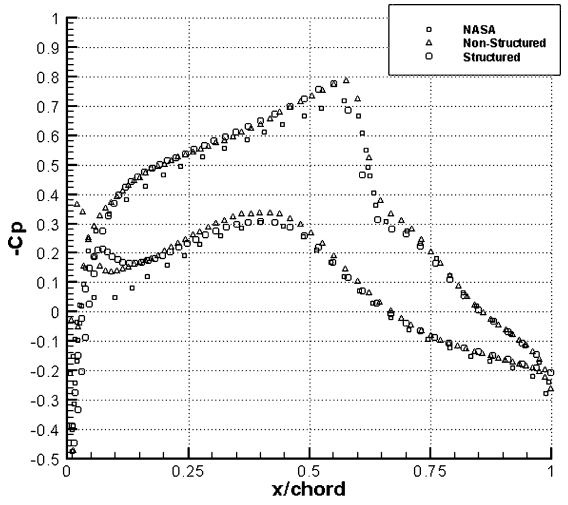

Fig. 4 C_p coefficients: a comparison with the results in Ref. 24.

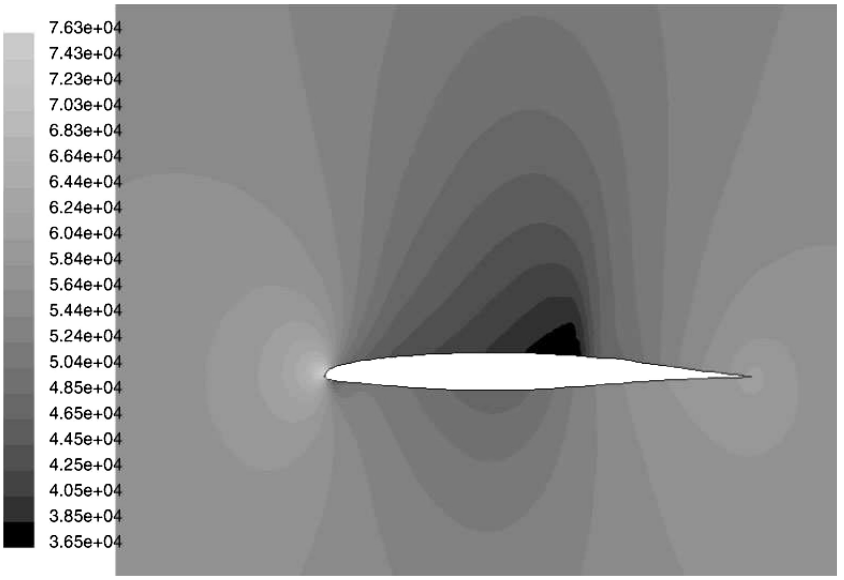

Fig. 3 MBB-A3 airfoil pressure field.

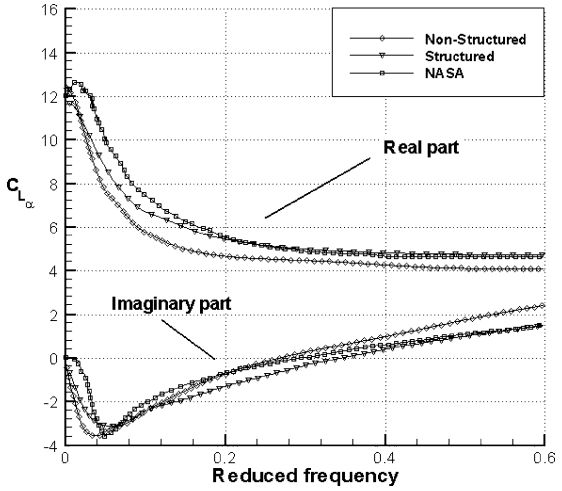

Fig. 5 Real and imaginary parts of C_{L_α} as function of reduced frequency k.

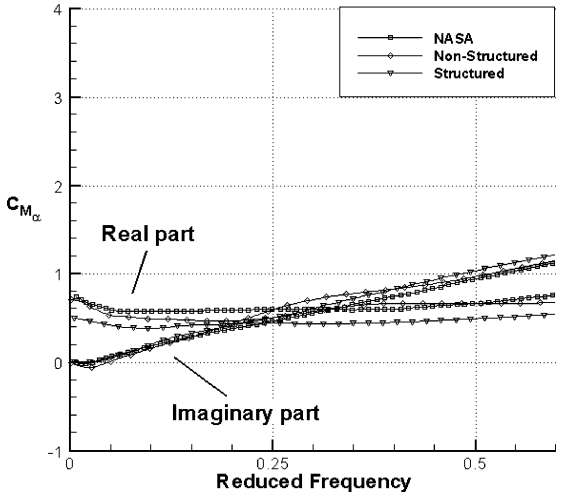

Fig. 6 Real and imaginary parts of C_{M_α} as function of reduced frequency k.

agreement with those given in Ref. 24 both for unstructured- and structured-mesh cases. However, the structured mesh gives results that are globally closer to that presented in Ref. 24.

Furthermore, an aeroelastic simulation using the same airfoil case has been performed to validate the considered procedure. Specifically, a local flutter solution analysis in transonic regime presented in Ref. 24 has been carried out considering the same structural and geometric parameters indicated. A dimensionless flutter speed of $U_F = 0.852$ and a flutter frequency of $k_F = 0.151$ have been obtained, and they are in very good agreement with the results presented in Ref. 24 for $M_\infty = 0.79$, which gives for the same quantities $U_F = 0.89$ and $k_F = 0.144$, respectively.

IV. Numerical Simulations for a LV

A. Linearized Structural Model

The structural dynamics of the VEGA LV have been studied using the MSC.NASTRAN commercial code. The structural model is based on a documented structural model for the LV. The FE dynamic model is based on a modeling of the Vega LV, in which every LV part is represented as a beam element characterized by an axial and a flexural stiffness. This kind of modeling allows the global distribution of mass and stiffness along the LV to be represented. The results of the modal analysis on the beam model are presented in Sec. IV.A.1. Section IV.A.2 shows the extrapolation procedure used to evaluate the modal displacement directly on the aerodynamic mesh surface. This issue is quite relevant to impose the unsteady modal boundary conditions for the GAF matrix identification.

Table 1 First natural frequencies normalized (with respect to the first one) of the model of the LV used for the aeroelastic analysis

Mode	Normalized frequencies	Mode-shape type
1	1.00	First bending
2	1.00	First bending
3	2.16	Second bending
4	2.16	Second bending
5	3.37	Third bending
6	3.37	Third bending

1. *Beam-Model Modal Analysis*

The modal analysis has been performed for a reference flight condition corresponding to a mass configuration which is about 80% of the initial liftoff mass configuration (which is about 135,000 kg for this LV). This condition is reached approximately 20 s after launch. The LV is considered in free–free boundary conditions to simulate the flight phase. Table 1 shows the first six normalized eigenfrequencies of the first three bending modes vibrating in two orthogonal transverse directions. Figure 7 shows the mode shapes of the first six natural modes. Specifically, the first two modes (Fig. 7a) have the same frequency because of the symmetry of the launcher, and they represent the first bending mode in two orthogonal transverse directions. The third and the fourth modes (Fig. 7b) have, again, the same frequency for the same reason and represent the second bending mode in the two directions as well. Finally, the fifth and the sixth modes (Fig. 7c) represent the third bending mode in the two orthogonal directions. These last two modes, which present a relatively large displacement on the LV nose, will be denoted in the following as "fairing" modes. Because of their special displacement nature, they might be relevant in the fluid-structure interaction mechanism. Indeed, they can produce a sudden increase of the local incidence with a possible significant flow perturbation and a possible onset of aeroelastic instabilities. Therefore, the first six modes have been included in this aeroelastic analysis. For the sake of simplicity, in the following aeroelastic applications the first two modes will be directly denoted as first mode, the third and the fourth modes as second mode, and the last two fairing modes as third mode.

2. *Expansion of the Mode Shapes on the Aerodynamic Mesh*

Once the displacement field given by the modal shape has been obtained for the one-dimensional structural model, it is necessary to define the same field also for the three-dimensional aerodynamic mesh. Indeed, to complete the definition of the linearized aeroelastic model, it is necessary to (see also Sec. IV.B) 1) impose every modal shape as an unsteady boundary condition to the CFD solver and 2) project the obtained pressure coefficient field on the body surface for each mode shape function [see Eq. (4)].

For the first item, a dynamic-mesh dedicated package of the CFD solver has been used. Therefore, the mode shape obtained from the beam model has been projected to the LV surface.

The base hypothesis of the data interpolation strategy is that any section orthogonal to the symmetry axis remains rigid during the motion. (This is consistent with the beamlike behavior of the LV model.) Furthermore, a linearized kinematics for the motion of the rigid sections has been assumed in the relationships relating the modal displacements and rotations of the beam model nodes and the displacements on the LV surface points. An example of the first mode displacement field on the three-dimensional VEGA LV is depicted in Fig. 8. The interpolation has been performed both on the centers of the aerodynamic surface panel elements for the force projection and on the nodes of the same aerodynamic surface panel for imposing the unsteady boundary conditions.

B. Vega LV Geometry and Steady-State Results

A structured mesh has been generally employed to study the steady and unsteady aerodynamic of the Vega LV. An important constraint to be satisfied using the structured mesh is the numerical stability of the solver during the mesh motion. The effect of

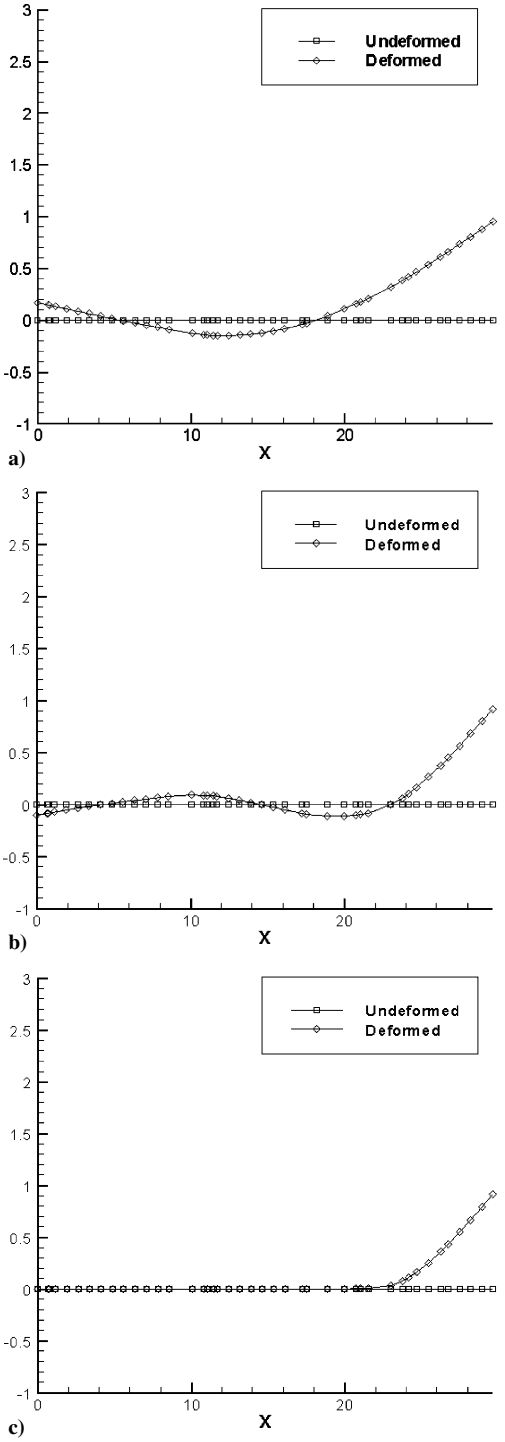

Fig. 7 Beamlike mode shapes of a) modes 1 and 2, b) modes 3 and 4, and c) modes 5 and 6.

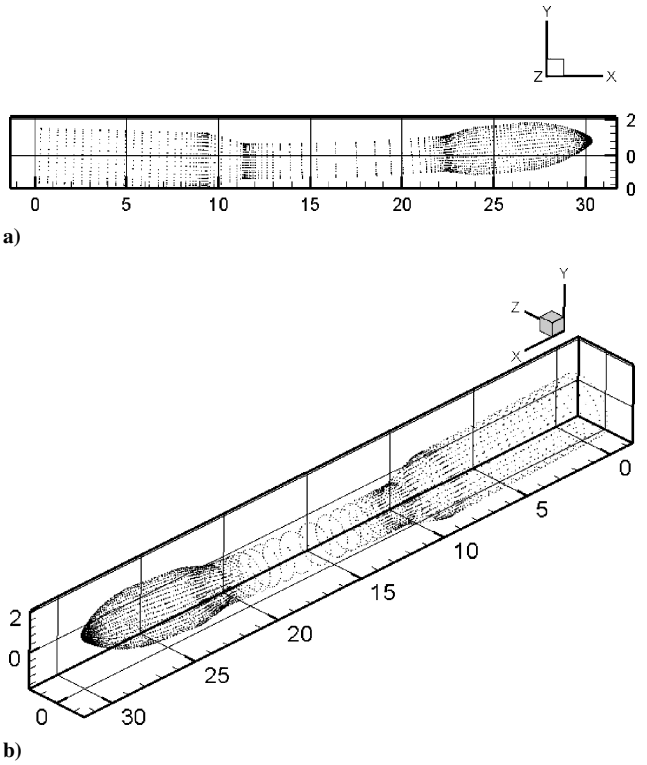

Fig. 8 Views of the first mode on the aerodynamic surface: a) two dimensional and b) three dimensional.

small perturbations on the unsteady boundary conditions has been checked to ensure the consequent deformation of the structured mesh does not significantly affect the mesh performance. Therefore, a structured mesh has been considered with the exception of the zone in the neighborhood of the LV nose up, where an unstructured mesh has been used. In this critical region, an unstructured mesh with quadrilateral elements has been used. A mesh-sensitivity study has been performed on the steady global aerodynamic axial force. (Similar results have been obtained for the other global LV aerodynamic loads such as normal force and pitching moment.) Representing the number of the volume elements by N_j and the corresponding computed axial load by C_{a_j}, the following results are obtained: ($N_1 = 10{,}350$, $C_{a_1} = 0.557$), ($N_2 = 35{,}000$, $C_{a_2} = 0.516$), ($N_3 = 76{,}930$, $C_{a_3} = 0.486$), ($N_4 = 260{,}350$, $C_{a_4} = 0.450$), and ($N_5 = 615{,}450$, $C_{a_5} = 0.434$). The mesh corresponding to N_3 has been considered as the reference mesh. The other meshes are obtained by homogeneously covering the same volume with proportionally decreased or increased number of points in each of the three coordinate directions. For example, meshes 1 and 2 have reduced resolution with 50 and 75% of the number of points in each direction compared with the reference mesh 3 (i.e., $N_1 = 76{,}930 \times 0.5 \times 0.5 \times 0.5 = 10{,}350$). Meshes 4 and 5 have increased resolution with 150% and 200% more points, respectively, than mesh 3 in each of the coordinate directions. Reference mesh 3 has been optimized with a local mesh refinement to obtain a pressure distribution on the LV lateral surface as much as possible similar to the data preexisting in the AVIO aerodynamic database and to the steady solutions obtained using more refined meshes, that is, giving a global aerodynamic axial load within the 8% of the converged value. The final aerodynamic structured reference mesh 3 is presented in Fig. 1. This optimized mesh has been successively refined and coarsened in order to perform the mesh sensitivity analysis. The fluid domain is truncated at the base of the launcher. This preserves the numerical stability of the solver (because of the recirculation zones on the LV base) and avoids the introduction of wake effects very different with respect to real operative condition with working engine. The mesh is characterized by different zone fitting. There is a fine grid near the launcher surface and a more rarefied zone at the extreme boundary of fluid domain. The strategy is to describe in detail the critical aerodynamic zones (launcher surface with remarkable variation of geometry, fairing zone) with saving on the total number of cells used. This improves significantly the efficiency of simulation, optimizing the ratio time/accuracy. The resulting mesh on half-body was specifically characterized by a number of mesh nodes of about 85,000, a number of faces (on half-launcher) of about 3300, a minimum aerodynamic face area equal to 1.423946×10^{-4} m^2, a minimum cell volume equal to 6.119432×10^{-6} m^3, and a cell height on the body surface equal to 0.0363665 m.

The trend of the global Reynolds number during atmospheric flight of the LV has been estimated, and the flight condition with the maximum Reynolds number (and lowest viscous effects) has been

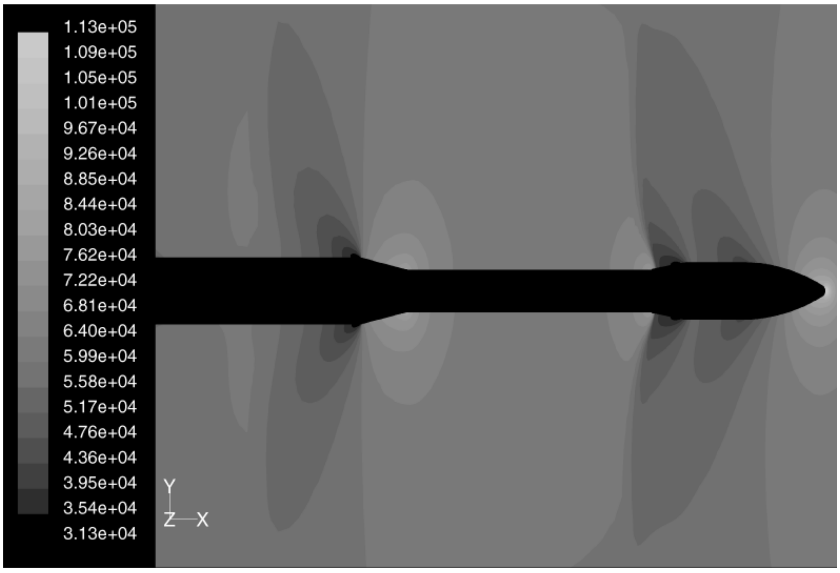

Fig. 9 Steady pressure distribution in the LV near field.

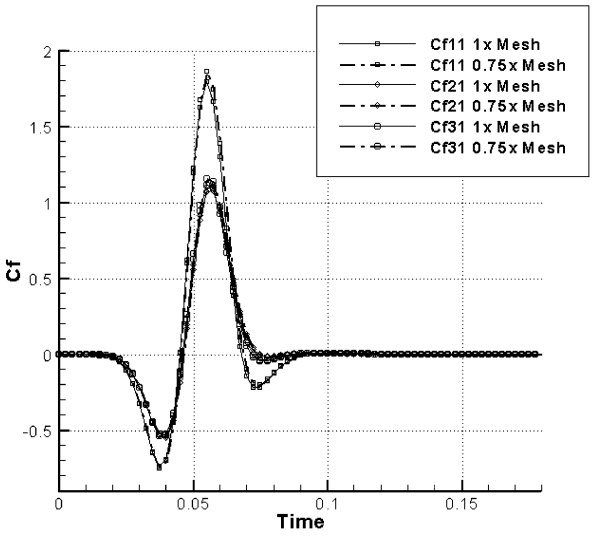

Fig. 10 Sensitivity analysis results. Generalized aerodynamic forces induced by the motion of mode 1 and projected to the mode shapes 1 (Cf 11), 2 (Cf 21), and 3 (Cf 31) for two different meshing strategies.

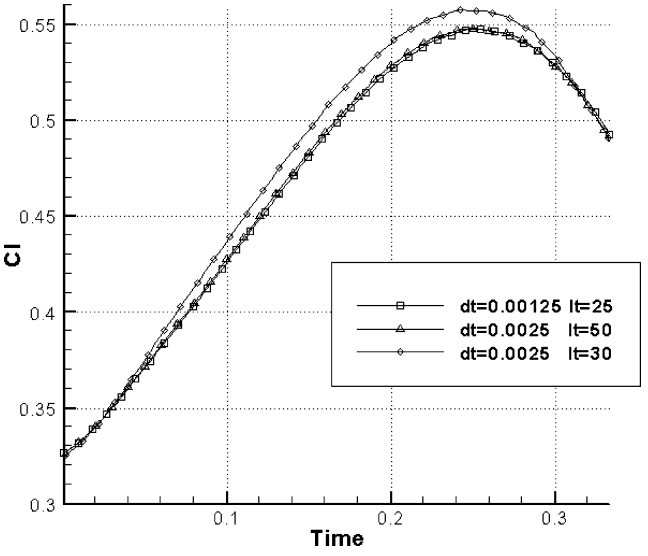

Fig. 11 Sensitivity analysis results. Unsteady lift coefficient due to a rigid LV pitch input.

selected for the current study. This flight segment is representative of the worst case for dynamic aeroelasticity of the LV. (This is similar, in some ways, to considering the maximum dynamic pressure as the worst case for static aeroelasticity.) This flow condition also enables us to use an Euler model (which, of course, does not consider viscous effects at all) to perform the aerodynamics simulations. The selected critical flow corresponds to a flight condition with Mach number $M_\infty = 0.98$ and $V_\infty = 326.43$ m/s. Also the critical condition for the reference steady angle of attack has been fixed to $\alpha = 1$ deg. The corresponding reference aerodynamic field is then calculated using the Euler-based implicit steady solver available in the FLUENT code. The predicted pressure distribution in this reference condition is presented in Fig. 9.

C. Unsteady Aerodynamic Results

A grid-sensitivity analysis for the unsteady case has been performed considering a comparison between the reference mesh (ratio 1) and the coarser mesh with ratio 0.75 presented in Sec. IV.B. The results, in term of generalized force responses in time domain, are depicted Fig. 10. The figure shows the generalized forces projected on the first (Cf 11), the second (Cf 21), and the third (Cf 31) modes (no repetition for transversally orthogonal modes is considered) as a result of an unsteady pulse motion of the first mode. The variation between the 1 and 0.75 mesh is of maximum a 4% for the amplitude of the time response (the same presented in the steady case), and no significant variations can seen for the phase shift. To have a global quantitative evaluation of such a difference, the standard deviations between the time histories given by the two different mesh have been evaluated ($\sigma_{Cf11} = 0.0066$, $\sigma_{Cf21} = 0.0030$, and $\sigma_{Cf31} = 0.0037$).

The sensitivity of time step and inner iteration number for each time step have been performed based on a simple simulation for a pitch motion of the launcher with respect to the mass center. The simulation is performed with different values of time step (TS) and iteration number for each time step (NTS). The chosen values are 1) TS = 0.00125 s and NTS = 25; 2) TS = 0.0025 s and NTS = 50; and 3) TS = 0.0025 s and NTS = 30. The results in terms of the lift coefficient are presented in Fig. 11. The simulation 1) and 2) have the best accuracy although they require greater CPU time. The order of the error in simulation 3) is less than 5% with respect to the other ones. This has justified the setup parameter of simulation 3) for the aeroelastic analysis.

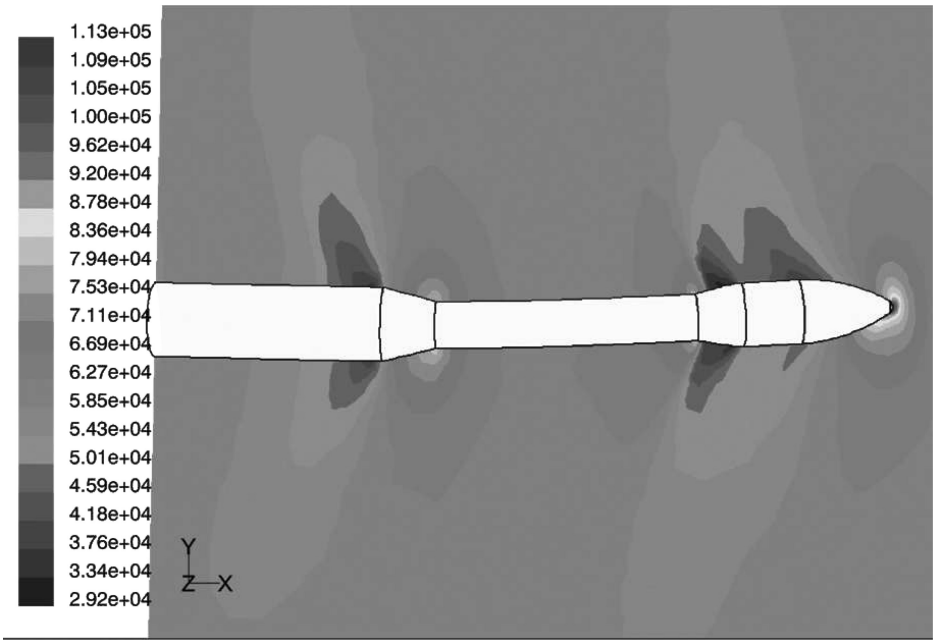

Fig. 12 Unsteady pressure distribution (maximum pressure values reached in time are represented) due to the motion of mode shape 1 with time input given by Fig. 2.

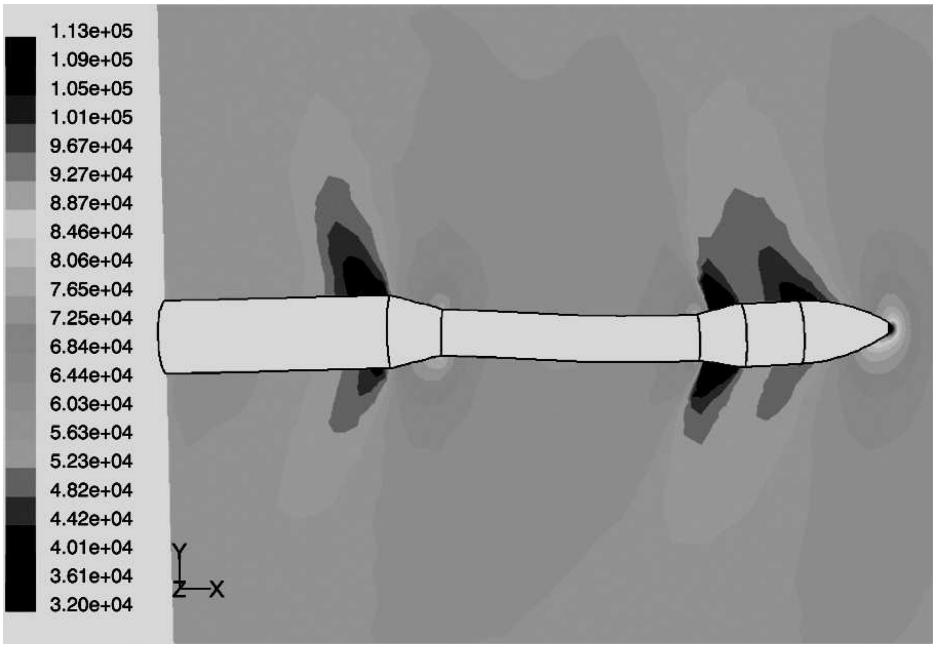

Fig. 13 Unsteady pressure distribution (maximum pressure values reached in time are represented) due to the motion of mode shape 2 with time input given by Fig. 2.

The trial-test characteristic parameters can be determined considering the bandwidth of interest of the unsteady phenomenon (which can be easily evaluated considering the maximum natural frequency considered in the structural modeling) and the numerical stability of the mesh with respect to the perturbations induced by the applied unsteady boundary conditions (specifically, a maximum local perturbation of angle of attack of 3 deg). Thus, three suitable trial-test time functions (one for each mode) have been determined.

The consequent direct CFD simulation with modal-shape-based motion in FLUENT supplies the unsteady pressure coefficient. The coefficient-pressure field at the time when the input function (see Fig. 2) reaches its maximum is shown in Figs. 12–14 for the three assumed mode shapes, respectively. These coefficients, filtered out of their steady component, have been projected on any assumed modal shape. The resulting generalized Lagrangian forces in time domain have been calculated for all of the assumed six modes. However, the effect of motion associated to one mode on the generalized aerodynamic force obtained projecting the induced unsteady pressure field on the corresponding orthogonal transverse mode proved to be quite negligible. This indicated that the aerodynamic coupling, potentially arising between transverse orthogonal modes in presence of a reference steady angle of attack of 1 deg, is negligible. For this reason only a reduced 3×3 GAF matrix has been considered in the aeroelastic analysis, that is, only three essential modes with displacements belonging to one plane only are considered in the analysis, and they will be denoted in the following as first, second, and third modes. (Incidentally, an aeroelastic analysis including all of the 6×6 GAF matrix terms has been also performed, but it gave the same stability results that will be presented in the next section.)

The resulting generalized Lagrangian forces in time domain are depicted in Figs. 15–17. In these figures, the second index is the number relative to the modal shape used for the boundary condition

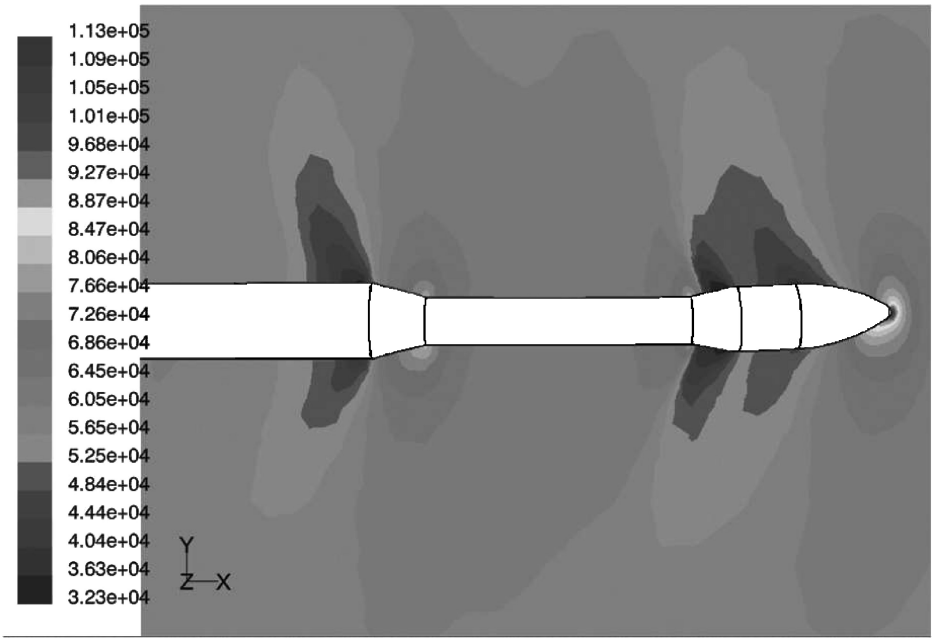

Fig. 14 Unsteady pressure distribution (maximum pressure values reached in time are represented) due to the motion of mode shape 3 with time input given by Fig. 2.

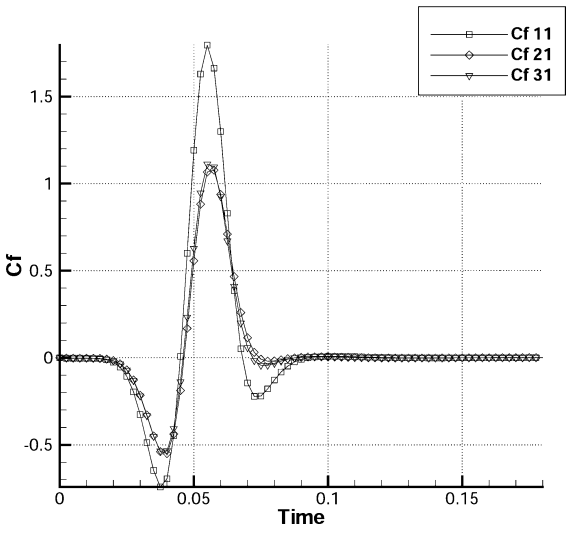

Fig. 15 Generalized aerodynamic forces induced by the motion of mode 1 and projected to the mode shapes 1 (Cf 11), 2 (Cf 21), and 3 (Cf 31).

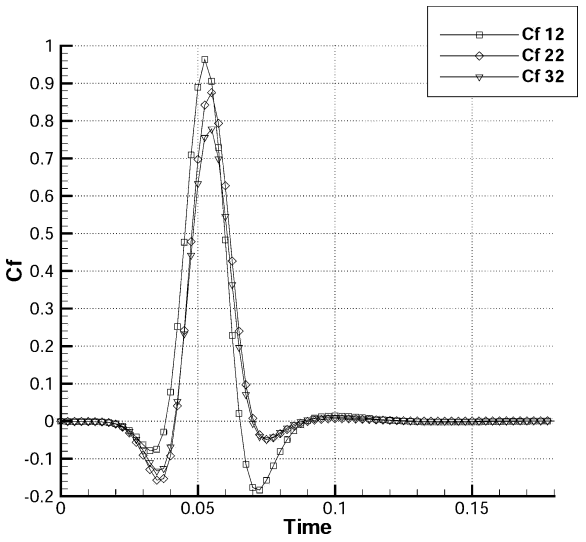

Fig. 16 Generalized aerodynamic forces induced by the motion of mode 2 and projected to the mode shapes 1 (Cf 12), 2 (Cf 22), and 3 (Cf 32).

in the CFD simulation, whereas the first one is the modal shape where the unsteady pressure fields are projected.

The generalized forces are transformed in frequency domain with a fast-Fourier-transform algorithm, and then the entries of the GAF matrix are evaluated using Eq. (12) in the Fourier domain. Finally, the GAF matrix is synthesized by means of a matrix rational polynomial interpolation to obtain a state-space form for the complete aeroelastic system. Figures 18–20 show the real and the imaginary parts of the synthesized GAF matrix. The matrix interpolating structure given by Eq. (16) has provided the constant matrices $\boldsymbol{A}_2, \boldsymbol{A}_1, \boldsymbol{A}_0$, $\boldsymbol{B}$, $\boldsymbol{C}$, and $\boldsymbol{A}$ necessary to perform the consequent standard stability analysis on the first-order linear representation given by Eq. (18).

D. Dynamic Aeroelastic Stability

Once the structural and aerodynamic linearized models for the LV are defined as in the preceding sections, the eigenproblem associated to the linear ordinary differential equation Eq. (18) has been performed for the considered transonic flow conditions. Specifically, the following flight parameters have been considered for the linearized aeroelastic analysis: $M_\infty = 0.98$, flow speed $V_\infty = 326.4$ m/s, and air density of the unperturbed flow $\rho_\infty = 0.75$ kg/m^3. (The other aerodynamic condition is a reference steady angle of attack $\alpha = 1$ deg; see Sec. IV.B.) The obtained eigenvalues, having imaginary parts within a range compatible with the domain of satisfactory approximation for the GAF matrix (i.e., $0 < k < 1.1$, or $0 < \omega < 125$ rad/s; see Figs. 12–20), are depicted in Fig. 21. The corresponding damping ratios, defined as ratio between the real part and imaginary part of the eigenvalue changed in sign, are given by

$$\gamma_1 = 0.0088, \qquad \gamma_2 = 0.0053, \qquad \gamma_3 = 0.0098$$

Thus, the aeroelastic system exhibits dynamic stability at this flow condition. The aerodynamics have induced global stabilizing effects on the LV structure in the assumed flow condition. The original structural poles, which are marginally stable and composed of three couples of coincident poles, tend, because of aeroelastic effects,

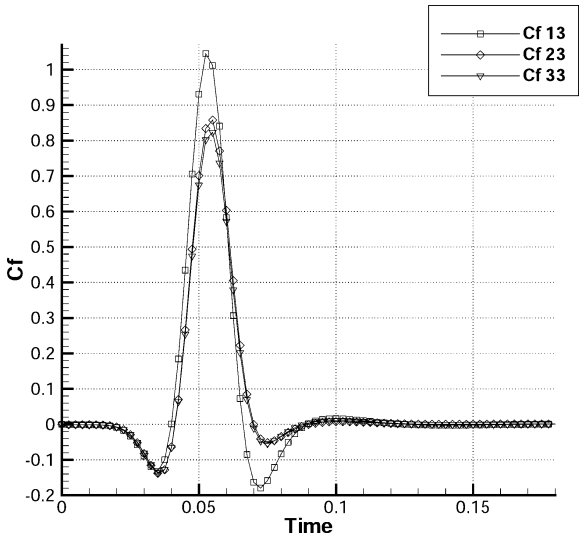

Fig. 17 Generalized aerodynamic forces induced by the motion of mode 3 and projected to the mode shapes 1 (Cf 13), 2 (Cf 23), and 3 (Cf 33).

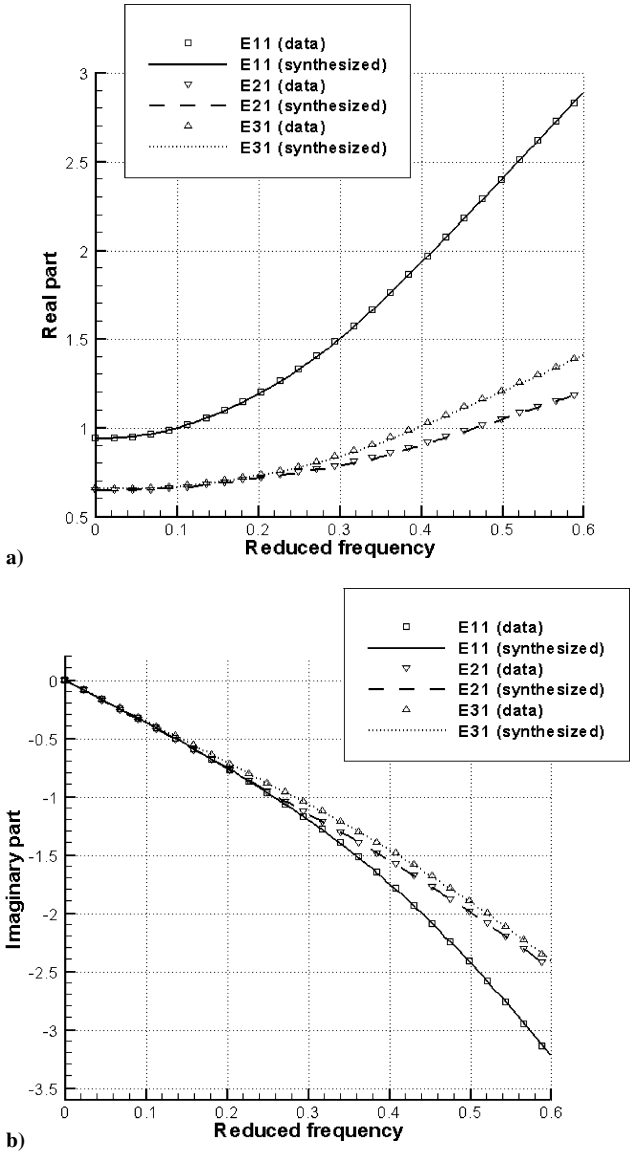

Fig. 18 Entries $E_{11}(k)$, $E_{21}(k)$, and $E_{31}(k)$ of GAF-matrix first column and their synthesized approximations: a) real and b) imaginary parts.

Table 2 Aeroelastic poles of the LV in transonic regime evaluated with different approaches

Aeroelastic pole	ROM approach	Iterative approach
1	$-2.37E-01+$i 26.82	$-2.11E-01+$i 26.85
2	$-3.24E-01+$i 60.84	$-2.92E-01+$i 60.90
3	$-7.22E-01+$i 73.86	$-8.26E-01+$i 73.77

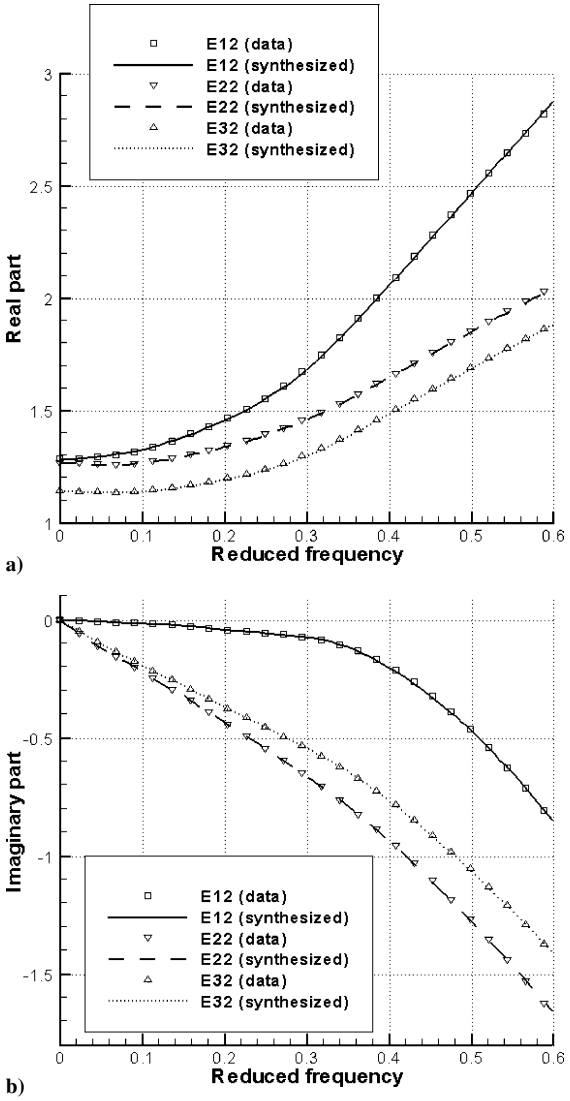

Fig. 19 Entries $E_{12}(k)$, $E_{22}(k)$, and $E_{32}(k)$ of GAF-matrix second column and their synthesized approximations: a) real and b) imaginary parts.

to decouple each other and to became more stable. This scenario is quantitatively described by the damping ratios just presented, which show that the fairing aeroelastic modes have a bit larger damping ratios than the others and that the second modes are less decoupled by the fluid/structure interaction.

Finally, an iterative procedure (see Sec. IV.B based on the *p–k* method[5]) to solve the nonlinear eigenvalue problem given by Eq. (14) has also been performed, and the obtained poles are compared with those given by the ROM procedure in Table 2. As one can see, the agreement between the different analyses is quite satisfactory.

E. Static Aeroelastic Stability

1. Simplified Aeroelastic Model: Slender-Body Theory

The slender-body-theory was originally introduced for airships aerodynamics and then extended to wings with very low aspect ratio.[26] The basic hypothesis of the theory is that the variation of

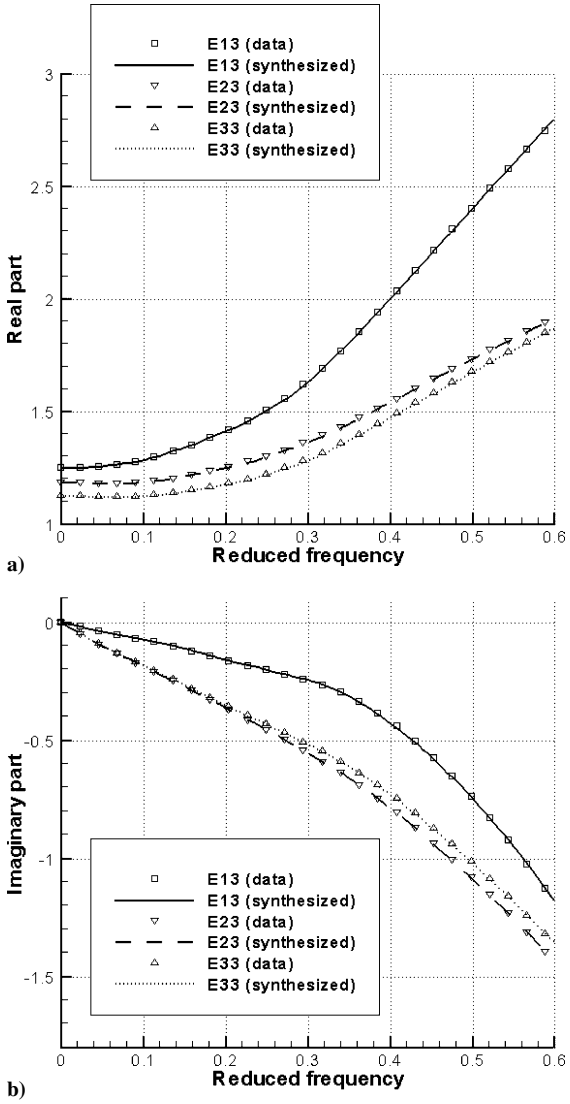

Fig. 20 Entries $E_{13}(k)$, $E_{23}(k)$, and $E_{33}(k)$ of GAF-matrix second column and their synthesized approximations: a) real and b) imaginary parts.

the geometric quantities of the body surface varies very slowly in one direction, for example, the axial direction x with respect to the other ones. The main results of this linearized theory are that the unsteady force orthogonal to the symmetry axis x is given by

$$L(x,t) = \rho_\infty \left(\frac{\partial}{\partial t} + V_\infty \frac{\partial}{\partial x} \right) [A(x)V(x,t)] \tag{19}$$

where $V(x,t)$ is the axial component of the flow that, following the same approximation of the theory, can be expressed as $V(x,t) = V_\infty \alpha(x,t)$, where $\alpha(x,t)$ is the local angle of the surface with respect to the axial direction. $A(x)$ represents the slowly varying (or constant) cross-sectional area along the length of the body.

Next, a static version of this operator has been considered in order to study only static aeroelastic phenomena like divergence. If the elastic body as simply described by the beam equation is considered, the aeroelasto-static equilibrium of the beam, using Eq. (19), is given by

$$\frac{\mathrm{d}^2}{\mathrm{d}x^2} \left(EI \frac{\mathrm{d}^2 w}{\mathrm{d}x^2} \right) = 2q_D \frac{\mathrm{d}}{\mathrm{d}x} \left[A(x) \left(\alpha_0 - \frac{\mathrm{d}w}{\mathrm{d}x} \right) \right] \tag{20}$$

where $w(x)$ is the beam bending displacement, EI is the local bending stiffness, and α_0 is the global angle of attack of the LV, which is a static term unessential to study the static stability.

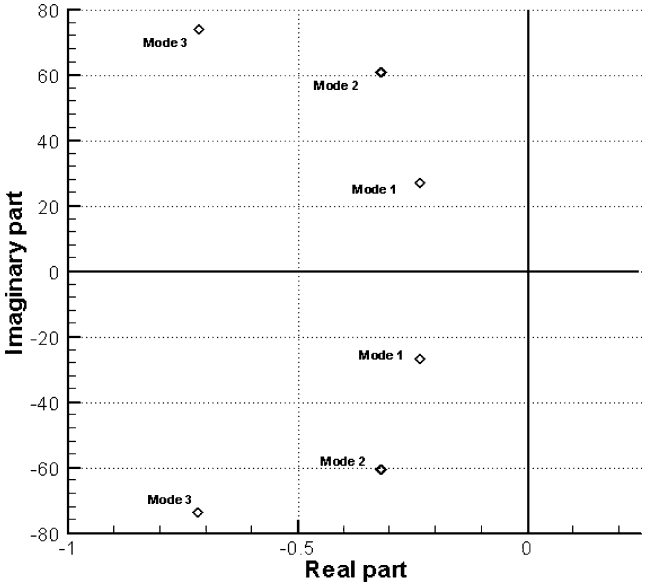

Fig. 21 Six eigenvalues (poles) of the aeroelastic system in the complex plane.

Equation (20) with the related boundary condition (free–free) has been discretized in the present work using a Galerkin procedure. Specifically, the first four beam analytical eigenmodes $\phi_n(x)$ of the free–free beam (with mass/stiffness characteristics constant with respect to x) have been assumed to build the solution

$$w(x) = \sum_{n=1}^{4} w_n \phi_n(x)$$

which is introduced in Eq. (20). After a standard Galerkin procedure, the resulting (discretized) algebraic system assumes the form

$$(\boldsymbol{K}_{\text{gal}} - q_D \boldsymbol{E}_0)\boldsymbol{w} = 0 \tag{21}$$

where $\boldsymbol{w}^T = \{w_1, w_2, w_3, w_4\}$ and the stiffness matrix and the (static) aerodynamic matrices are given by the projection procedure. Note that a standard eigenproblem performed directly on the matrices $\boldsymbol{K}_{\text{gal}}$ and $\boldsymbol{E}_0$ gives as eigenvalues, whenever positive, the critical value for the divergence dynamic pressure. [Note also that Eq. (21) is quite similar to Eq. (5) whenever the static phenomena, i.e., setting $s = 0$, were considered.]

2. Comparison with the Elementary Slender-Body Theory Results

The linear stability analysis presented in Sec. IV.E.1 is quite general and would include also possible static stability, that is, the presence of a zero eigenvalue. However, this kind of instability would occur for a flight or parametric situation, which is quite out of the range of the local parameters. The solution of the eigenvalue problem associated with the relationship $[\boldsymbol{K} - q_D \boldsymbol{E}(0)]\,\boldsymbol{q} = 0$ [see Eq. (5) when $s = 0$, i.e., a direct search of possible zero pole] has been performed. The smallest real eigenvalues can be directly considered as the critical value for the dynamic pressure of divergence. Moreover, the corresponding eigenvector gives, for any components, the contribution on static instability of each modes included in the analysis.

Using the GAF matrix presented, in static condition (i.e., when $k = 0$), a dedicated eigenproblem with eigenvalues with dimension of the dynamic pressure can be performed to achieve the static stability margin, that is, a possible divergence condition for the VEGA LV. The divergence instability is associated to the first mode shape with a corresponding divergence speed equal to $U_D = 1123$ m/s. This corresponds to a critical dynamical pressure equal to $q_D = 4.725E05$ Pa. However, these parameters do not indicate a real instability because they are far from the reference conditions considered in the local analysis.

Finally, a comparison of these results with those given by the simplified slender-body theory is presented. The eigenproblem associated with Eq. (21) has been solved considering only the first three beam analytical eigenmodes in the wind plane only. The smallest value, $q_D = 9.500E05$, physically represents dynamic pressure of divergence given by the slender-body theory. Hence this corresponds to $U_D = 1590.66$ m/s. Thus, the approximated theory gives an overestimation of the value computed by the present analysis, and, therefore, it seems to be conservative. However, this static instability limit is, again, quite out of the considered reference flight conditions.

V. Conclusions

The main objective of this paper is the proposal and the application of an unconventional approach for the study of the aeroelastic behavior of an LV in transonic flight condition.

The structural dynamic model uses a modal representation for the LV structure in terms of the first six natural frequencies and modes of vibration obtained via a FE solver. The linearized unsteady aerodynamic model has been obtained using the CFD data from an Euler-based code. The predicted aerodynamic data have been postprocessed to obtain a global generalized representation for the aerodynamic loads associated with the actual deformation state of the LV in terms of its modal description. The Lagrange equations describing the global aeroelastic behavior in terms of the six chosen modal coordinates have been obtained (after a suitable state-space reduction for the unsteady aerodynamics) as a set of linear ODEs with constant coefficients.

Finally, a standard eigenanalysis has been performed to check the static and dynamic aeroelastic stability of the Vega LV in the neighborhood of the transonic flight phase under investigation. The procedure has been also validated by means of a two-dimensional airfoil transonic aeroelastic analysis available in the literature. The generality of such a procedure allows one to apply the approach in the neighborhood of any arbitrary parametric flight condition of a LV.

Acknowledgment

This paper has been supported by a grant from AVIO S.p.A. and the Department of Aerospace Engineering and Astronautics of the University of Rome "La Sapienza" entitled "VEGA LV Launch Vehicle Aeroelastic Stability Analysis in Critical Transonic Flight Condition."

References

[1]Bisplinghoff, R. L., Ashley, H., and Halfman, R. L., *Aeroelasticity*, Addison Wesley Longman, Cambridge, MA, 1955, pp. 1–14, 527–626.

[2]Morino, L., "A General Theory of Unsteady Compressible Potential Aerodynamics," NASA CR-2464, Dec. 1974.

[3]Dowell, E. H., Crawley, E. F., Curtiss, H. C., Peters, D. A., Scanlan, R. H., and Sisto, F., *A Modern Course in Aeroelasticity*, Kluwer Academic, Dordrecht, The Netherlands, 1995, Chaps. 2–4.

[4]Silva, W. A., Hong, M. S., Bartel, L. E., Piatak, D. J., and Scott, R. C., "Identification of Computational and Experimental Reduced-Order Models," *Proceedings of International Forum on Aeroelasticity and Structural Dynamics* [CD-ROM], Netherlands Association of Aeronautical Engineers, Amsterdam, 2003, Paper US-39.

[5]Hassig, H. J., "An Approximate True Damping Solution of the Flutter Equation by Determinant Iteration," *Journal of Aircraft*, Vol. 8, No. 11, 1971, pp. 885–889.

[6]Venkatesan, C., and Friedmann, P. P., "New Approach to Finite-State Modeling of Unsteady Aerodynamics," *AIAA Journal*, Vol. 24, No. 12, 1986, pp. 1889–1897.

[7]Eversman, W., and Tewari, A., "Consistent Rational-Function Approximation for Unsteady Aerodynamics," *Journal of Aircraft*, Vol. 28, No. 9, 1991, pp. 545–552.

[8]Morino, L., Mastroddi, F., De Troia, R., Ghiringhelli, G. L., and Mantegazza, P., "Matrix Fraction Approach for Finite-State Aerodynamic Modeling," *AIAA Journal*, Vol. 33, No. 4, 1995, pp. 703–711.

[9]Gennaretti, M., and Lisandrin, P., "Flap-Lag Rotor Dynamics and Aeroelastic Stability Using Finite-State Aerodynamics," *Proceeding of 24th European Rotorcraft Forum*, Association Aéronautique et Astronautique de France, Marseilles, France, 1998, pp. DY.01.1–DY.01-11.

[10]Balis Crema, L., Mastroddi, F., and Coppotelli, G., "Aeroelastic Sensitivity Analyses for Flutter Speed and Gust Response," *Journal of Aircraft*, Vol. 37, No. 1, 2000, pp. 172–180.

[11]Gennaretti, M., and Mastroddi, F., "A Study of Reduced-Order Models for Gust-Response Analysis of Flexible Fixed Wing," *Journal of Aircraft*, Vol. 41, No. 2, 2004, pp. 304–313.

[12]Tsai, H. M., Wong, A. S. F., Lai, J., Zhu, Y., and Liu, F., "Unsteady Flow Calculations with a Parallel Multiblock Moving Mesh Algorithm," *AIAA Journal*, Vol. 39, No. 6, 2001, pp. 1021–1029.

[13]Thomas, J. P., Dowell, E. H., and Hall, K. C., "Nonlinear Inviscid Aerodynamics Effects on Transonic Divergence, Flutter and Limit-Cycle Oscillations," *AIAA Journal*, Vol. 40, No. 4, 2002, pp. 638–646.

[14]Ragab, M. M., "Buffet Loads Prediction for a Launch Vehicle and Comparison to Flight Data," *Journal of Spacecraft and Rockets*, Vol. 29, No. 6, 1992, pp. 849–855.

[15]Reding, P. J., and Ericsson, L. E., "Hammerhead and Nose-Cylinder-Flare Aeroelastic Stability Revisited," *Journal of Spacecraft and Rockets*, Vol. 32, No. 1, 1995, pp. 55–59.

[16]Dotson, K. W., Baker, R. L., and Sako, B. H., "Launch Vehicle Self-Sustained Oscillation from Aeroelastic Coupling Part 1: Theory," *Journal of Spacecraft and Rockets*, Vol. 35, No. 3, 1998, pp. 365–373.

[17]Dotson, K. W., Baker, R. L., and Bywater, R. J., "Launch Vehicle Self-Sustained Oscillation from Aeroelastic Coupling Part 2: Analysis," *Journal of Spacecraft and Rockets*, Vol. 35, No. 3, 1998, pp. 374–379.

[18]Karpel, M., Yaniv, S., and Livshits, D. S., "Integrated Solution for Computational Static Aeroelasticity of Rockets," *Journal of Spacecraft and Rockets*, Vol. 35, No. 5, 1998, pp. 612–618.

[19]Ericsson, L. E., "Hammerhead Wake Effects on Elastic Vehicle Dynamics," *Journal of Spacecraft and Rockets*, Vol. 34, No. 2, 2000, pp. 145–151.

[20]Ericsson, L. E., and Pavish, D., "Aeroelastic Vehicle Dynamics of a Proposed Delta II 7920-10L Launch Vehicle," *Journal of Spacecraft and Rockets*, Vol. 37, No. 1, 2000, pp. 28–38.

[21]Ericsson, L. E., "Unsteady Flow Separation can Endanger the Structural Integrity of Aerospace Launch Vehicle," *Journal of Spacecraft and Rockets*, Vol. 38, No. 2, 2001, pp. 168–179.

[22]FLUENT 6.1, User's Guide, Fluent, Inc., Lebanon, NH, Nov. 2001.

[23]"Experimental Data Base for Computer Program Assessment," AGARD AR-138, May 1979.

[24]Bland, S. R., and Edwards, J. W., "Airfoil Shape and Thickness Effects on Transonic Airloads and Flutter," NASA TM-84632, March 1983.

[25]GAMBIT 2.1, User's Guide, Fluent, Inc., Lebanon, NH, Nov. 2001.

[26]Paidoussis, M. P., *Fluid-Structure Interactions. Slender Structures and Axial Flow*, Vol. 1, Academic Press, San Diego, CA, 1998, pp. 26–36.

P. Weinacht
Associate Editor